Author Manuscript

Fibulin-3 knockout mice demonstrate corneal dysfunction but maintain normal retinal integrity

Steffi Daniel[1], **Marian Renwick**[1], **Viet Q. Chau**[1], **Shyamtanu Datta**[1,2], **Prabhavathi Maddineni**[3], **Gulab Zode**[3], **Emma M. Wade**[4], **Stephen P. Robertson**[4], **W. Matthew Petroll**[1], **John D. Hulleman**[1,5]

[1]Department of Ophthalmology, University of Texas Southwestern, Medical Center, 5323 Harry Hines Blvd, Dallas, TX, USA [2]Department of Ophthalmology, Schepens Eye Research Institute, Massachusetts Eye and Ear, Harvard Medical School, Boston, MA, USA [3]Department of Pharmacology and Neuroscience, University of North, Texas Health Science Center, 3500 Camp Bowie Blvd, Fort, Worth, TX, USA [4]Department of Women's and Children's Health, Dunedin School of Medicine, University of Otago, Dunedin 9016, New Zealand [5]Department of Pharmacology, University of Texas Southwestern, Medical Center, 5323 Harry Hines Blvd, Dallas, TX, USA

Abstract

Fibulin-3 (F3) is an extracellular matrix glycoprotein found in basement membranes across the body. An autosomal dominant R345W mutation in F3 causes a macular dystrophy resembling dry age-related macular degeneration (AMD), whereas genetic removal of wild-type (WT) F3 protects mice from sub-retinal pigment epithelium (RPE) deposit formation. These observations suggest that F3 is a protein which can regulate pathogenic sub-RPE deposit formation in the eye. Yet the precise role of WT F3 within the eye is still largely unknown. We found that F3 is expressed throughout the mouse eye (cornea, trabecular meshwork (TM) ring, neural retina, RPE/choroid, and optic nerve). We next performed a thorough structural and functional characterization of each of these tissues in WT and homozygous (F3−/−) knockout mice. The corneal stroma in F3−/− mice progressively thins beginning at 2 months, and the development of corneal opacity and vascularization starts at 9 months, which worsens with age. However, in all other tissues (TM, neural retina, RPE, and optic nerve), gross structural anatomy and functionality were similar across WT and F3−/− mice when evaluated using SD-OCT, histological analyses, electron microscopy, scotopic electroretinogram, optokinetic response, and axonal anterograde transport. The lack of noticeable retinal abnormalities in F3−/− mice was confirmed in a human patient with biallelic loss-of-function mutations in F3. These data suggest that (i) F3 is important for maintaining the structural integrity of the cornea, (ii) absence of F3 does not affect the structure or function of any other ocular tissue in which it is expressed, and (iii) targeted silencing of F3 in the retina and/or RPE will likely be well-tolerated, serving as a safe therapeutic strategy for reducing sub-RPE deposit formation in disease.

Introduction

Fibulin-3 (aka EFEMP1 or F3 (used hereafter)) is a 55 kDa, disulfide-rich secreted extracellular matrix glycoprotein belonging to the fibulin family of proteins and is broadly expressed in epithelial and endothelial cells across the body. Structurally, it is comprised of tandem arrays of calcium-binding epidermal growth factor (EGF) domains and a carboxy-terminal fibulin-type module [1, 2]. It is highly conserved among different species with 92–94% homology between humans and rodents. Although the exact function of F3 is unknown, studies suggest that it might be involved in elastogenesis and may play an important role in the development and maintenance of connective tissue [3–5]. F3 has also been associated with several cancers; however, its role in cancer development is contradictory as it has been reported to be both anti- and pro-neoplastic, depending on tissue context [6–9].

Studies suggest that the accumulation of F3 may alter extracellular matrix (ECM) homeostasis by interacting with the basement membrane proteins such as tissue inhibitor of metalloproteinase-3 (TIMP-3) [10], matrix metalloproteinases (MMPs) [10], collagen XV [11], collagen XVIII/endostatin [11], or even ECM regulatory proteins such as transforming growth factor beta-2 (TGFβ2) [12]. Consistent with the notion of F3 being expressed in adult retina and the developing retina of humans and rodents [13] as well as being an important regulator of the ECM, a single arginine-to-tryptophan (Arg345Trp [p.R345W]) missense mutation in F3 leads to a rare, gain-of-function, autosomal dominant macular dystrophy called Malattia Leventinese (ML) [14]. ML is characterized by early onset drusen formation that leads to progressive and irreversible vision loss, with symptoms typically presenting during the third or fourth decade of life [15, 16]. In cell culture studies, R345W F3 displays significant secretion defects, indicating that this mutation likely leads to protein misfolding and accumulation of F3 within RPE cells [17–22] and disruption of the complement system [23]. In mice, this mutation triggers the progressive formation of membrane-rich basal laminar deposits (BLamDs) [24, 25], again potentially through complement system disruption [23, 26]. Yet, it is clear that F3 is also an important player in more common ocular diseases such as age-related macular degeneration (AMD) [2]. Aside from the observation that an Asp49Ala (D49A) mutation in F3 was associated with a cuticular drusen subtype of AMD [27], additional studies have found that WT F3 surrounds drusen in individuals with AMD [28]and that copy number variation near the F3 locus is correlated with an increased likelihood of AMD [29]. Furthermore, an Arg140Trp (R140W) mutation in F3 associated with primary open-angle glaucoma [30] suggests that F3 may play an important role in ocular tissues beyond the retina/RPE.

Recent data characterizing patients with loss-of-function F3 variations (one individual with biallelic mutations [31], and two siblings with a homozygous C55R missense mutation in F3 [32]) have been reported to manifest aging phenotypes like scoliosis, deformed bones,

multiple hernias, myopia, and astigmatism. Intriguingly, the primary phenotypes of F3 knockout (F3−/−) mice also include premature aging phenotypes such as reduced lifespan, muscle/organ atrophy, hernias, and pelvic prolapse [3, 33]. Yet, using basic histology and electron microscopy, no obvious RPE/Bruch's membrane–related pathological changes (i.e., sub-RPE deposits or BLamDs) were observed in these F3−/− mice [3]. In fact, later studies showed that knocking out F3 prevented environmentally induced BLamD formation [34]. These studies are exciting in that they suggest that F3 plays a crucial role in sub-RPE deposit/BLamD formation and that silencing or knocking out F3 through gene therapy could be a therapeutic approach for treating ML, and possibly AMD. However, given its apparent broad expression in the corneal epithelium, ciliary body, nerve fiber layer, retina, and optic nerve head [1], absence of F3 may cause unwanted side effects which would supersede targeting F3 as a therapeutic strategy.

Therefore, in the current study, we utilized C57BL/6 mice to first quantitatively evaluate the relative expression of F3 in various bodily and ocular tissues. Subsequently, we performed an extensive and thorough study to understand the role of F3 in the eye by characterizing wild-type (WT), heterozygous (F3+/−), and F3−/− mice with respect to their corneal anatomy by in vivo confocal microscopy and slit-lamp imaging; retinal layer thickness and volume measurements by Spectral Domain-Optical Coherence Tomography (SD-OCT); response to light stimuli by electroretinogram (ERG); visual acuity by measuring optokinetic reflex (OKR); and retinal, corneal, and optic nerve histology by Hematoxylin and Eosin (H&E) staining, immunohistochemistry (IHC), and transmission electron microscopy (TEM).

Through these studies, we have attempted to understand the role of F3 in maintaining ocular homeostasis and how the absence of F3 affects the overall structure and function of the eye. We demonstrate that in the absence of F3, the highly organized structural assembly in the cornea is disturbed, leading to pathological changes, demonstrating that F3 is crucial for maintaining homeostasis in the mouse cornea. However, the loss of F3 does not have any detrimental effects on other ocular tissues investigated in these studies. These data are a promising step forward that provide an ocular safety profile for removal of F3 and pave the way for the development of a retina/RPE-centered F3-based gene knockdown/out strategy for diseases like ML and possibly AMD.

Results

Fibulins are redundant yet tissue-specific in expression

While it is known that members of the fibulin family of proteins are involved in a variety of developmental, physiological, and pathophysiological processes [4, 35–37], to our knowledge, a side-by-side quantitative comparison of their gene expression profiles from diverse tissues has never been performed. Thus, we initiated our study by profiling the expression of fibulin-1 through fibulin-5 (F1–F5) in a variety of adult WT C57BL/6 mouse tissues (heart, lung, brain, testes, uterus, and posterior eye cup (containing the neural retina and the RPE/choroid vasculature)). We found that the expression of fibulin genes overlapped, yet also demonstrated tissue specificity in particular instances (Fig. 1a). For example, high levels of F1 expression were observed in the heart and uterus, whereas F2 was

minimally expressed in every tissue compared with other fibulins (except in the uterus where it is expressed abundantly). F4 and F5 displayed comparable patterns of expression in most of the tissues. Among the analyzed fibulins, we observed that F3 expression was considerably high in the lung, testes, and posterior eye cup (Fig. 1a).

Due to the association of fibulin mutations with ocular disease (i.e., in F3 and F5), we next focused on the expression of fibulins specifically in ocular tissues (Fig. 1b). We found that F1 was predominantly expressed in most of the ocular tissues except the cornea and neural retina. Low levels of F2 were observed in most ocular tissues, consistent with observations made in other tissues in the body (Fig. 1a). Whereas F4 and F5 were predominantly expressed in the RPE/choroid, F3 was largely expressed in the cornea, trabecular meshwork (TM) ring, neural retina, and optic nerve (Fig. 1b). Incidentally, the expression of F3 was actually lowest in the RPE/choroid compared with that of all other ocular tissues (Fig. 1c). This observation was surprising, especially since experiments focused on F3 are routinely framed from the perspective of RPE biology and pathophysiology. Nevertheless, our results do not preclude the importance of F3 in the RPE/choroid, but rather peaked our curiosity to evaluate the kind of role(s) F3 might play in other ocular tissues where it is highly expressed. These results, combined with indications of F3's involvement in a number of diverse ocular disorders ranging from ML to AMD to POAG, led us to explore the functional consequences of its absence in the mouse eye.

F3 is crucial for maintaining corneal integrity

Since F3 is the predominant fibulin found in the mouse cornea (Fig. 1b), we began our characterization of F3+/− and F3−/− mice by performing corneal in vivo confocal imaging. Qualitative assessment of confocal images did not reveal any differences in cell morphology within the epithelium, stroma, or endothelium (Fig. 2a). Quantitative analysis was performed to evaluate changes in epithelial cell size, stromal backscatter (intensity), and stromal thickness. Corneal scans in 2-month-old mice revealed no significant differences in epithelial cell sizes (Fig. 2b, WT 1529 ± 133.6 μm^2, F3+/− 1549 ± 201.9 μm^2, and F3−/− 1597 ± 164.5 μm^2)(n =7–12) as well as stromal backscatter (Fig. 2c, WT 39.4 ± 3.8 AU, F3+/− 42.1 ± 2.8 AU, and F3−/− 39.2 ± 3.2 AU)(n =7–12). However, a significant reduction in stromal thickness was observed in F3−/− animals compared to WT (Fig. 2d, WT 58.1 ± 4.7 μm, F3+/− 56.6 ± 7.2 μm, and F3−/− 50.9 ± 8.4 μm) (n =7–12, p = 0.02, 2-way ANOVA). Even by 6 months of age, no significant changes were observed in epithelial cell sizes among animals (Fig. 2b, WT 1615.4 ± 162.8 μm^2, F3+/− 1690.2 ± 58.9 μm^2, and F3−/− 1613.9 ± 291.1 μm^2)(n =4–7). However, increased stromal backscatter (Fig. 2c, WT 40.3 ± 3 AU, F3+/− 47.0 ± 6.2 AU, and F3−/− 65.3 ± 6.2 AU)(n =4–7, p < 0.0001, 2-way ANOVA) as well as progressive stromal thinning was observed in F3−/− animals compared with that in WT (Fig. 2d, WT 63.5 ± 3.5 μm, F3+/− 56.2 ± 6.1 μm, and F3−/− 45 ± 5 μm)(n =4–7, p < 0.001, 2-way ANOVA). We did not observe differences between F3+/− and WT animals in any of these analyses at 2 months or 6 months, suggesting that a single copy of F3 is sufficient to maintain corneal integrity.

Macroscopic corneal changes began to manifest in F3−/− animals as early as 9 months. These changes included increased corneal opacity and vascularization that progressively

worsened with age (observations made through 15 months), and frequently prevented us from in vivo assessment of structure or function of the F3−/− mice at time points > 9 months (as described below). Corneal changes manifested with varying degrees of severity as observed through slit-lamp imaging (Fig. 3a). Histological cross sections of the cornea at 12 and 15 months also confirmed stromal thinning and disruption due to the presence of blood vessels in F3−/− (Fig. 3b), further emphasizing the importance of F3 in the mouse cornea, especially with increasing age.

The macroscopic changes and vascularization observed in F3−/− corneas by 9 months could be caused by a loss of limbal integrity. Therefore, we evaluated whether absence of F3 caused a noticeable reduction of corneal stem cells and general proliferation in the limbus. Using limbal stem cell (K15 [38]) and proliferation markers (Ki67 [39]), we examined both WT and F3−/− corneas in 8-month mice, an age on the cusp of initial noticeable opacification. We observed similar numbers of Ki67-positive limbal stem cells present in WT and F3−/− animals (Supp. Fig. 2). Moreover, both WT and F3−/− corneas exhibit K15-positive, actively proliferating cells (Supp. Fig. 2). These data suggest that the absence of, or a noticeable reduction in corneal stem cells or their proliferation is not the primary reason for the corneal changes detected in F3−/− animals. Alternatively, these results support the idea that absence of F3 likely leads to dysfunction in the corneal epithelium or the ECM of the stroma.

Loss of F3 does not affect the structural anatomy of other ocular tissues including the ciliary body, retina, RPE, and optic nerve

High expression levels of F3 were observed in the TM ring, neural retina, and optic nerve. F3 is believed to be responsible for providing structure and support to various tissues in the body. Therefore, we closely examined the ocular tissues where F3 is highly expressed for structural changes in the absence of F3. Both the ciliary body and TM play a role in intraocular pressure (IOP) control. The ciliary body produces the aqueous humor, while the TM is responsible for its drainage. Changes in the aqueous humor dynamics alter IOP and cause mechanical stress to the retina that might lead to glaucomatous changes [40]. However, in our study, histological analyses of the TM and ciliary body showed no abnormalities in the F3−/− mice compared with that in WT at 15 months (Supp. Fig 3a).

Our qPCR data and a prior in situ hybridization experiment [30] show strong evidence of F3 expression in the neural retina and optic nerve. We next performed a thorough structural analysis to determine changes in the neural retina in the absence of F3. Upon SD-OCT examination, the various retinal layers of WT and F3−/− animals were nearly identical in thickness at 9 months (Fig. 4a, b). SD-OCT on F3−/− mice at later time points > 9 months was not feasible due to opacification of the cornea. Therefore, we performed histological comparison by H&E, which confirmed no structural abnormalities between WT of F3−/− mice or changes in the different retinal layers at 12 and 15 months (Fig. 4c).

Given the recent observation that the R345W mutant of F3 may cause changes to the intrinsically photosensitive retinal ganglion cells (ipRGCs) [41], and that there is an apparently high level of F3 produced in mouse RGCs (Supp. Fig. 3b), we decided to assess RGC density in WT and F3−/− mice. Immunolabeling of the ganglion cells revealed no

differences in densities between WT and F3−/− animals (Fig. 5a, b; WT= 2265 ± 135 cells/mm^2, F3−/− = 2303 ± 94 cells/mm^2) at15 months (n =5–6). Moreover, as F3 has been shown to be associated with complement factor H (CFH) [42], which is a key modulator of immunity through regulation of the alternative pathway of the complement system, we determined whether lack of F3 led to any glial cell changes in the retina. We immunolabeled for astrocytes (GFAP) and microglia (Iba-1) and compared WT with F3−/− retinas in 8 month mice (Supp. Fig. 4a–d). No significant differences were observed in the levels of astrocytes (Supp. Fig. 4a, b; WT = 19.73 ± 2.93 AU, F3−/− = 19.34 ± 2.17 AU, n = 4) or microglia (Supp. Fig. 4c, d; inner retina WT = 199 ± 17 cells/mm^2, F3−/− = 186 ± 19 cells/mm^2, outer retina WT = 169 ± 35 cells/mm^2, F3−/− = 176 ± 41 cells/mm^2, n = 4) at 8 months. Optic nerve cross sections showed healthy axons and no glial or fibrotic changes in the absence of F3. Axonal quantification in the F3−/− mice was also comparable with that in the WT (WT = 4.7 ± 0.7 × 10^5 axons/mm^2, F3−/− = 4.4 ± 0.5 × 10^5 axons/mm^2) at 15months (n = 3–4) (Fig. 5c, d).

Considering the association of WT [19] and R345W [19, 24] F3 with sub-RPE/basal laminar deposits and disruption of the RPE/Bruch's membrane, we next evaluated RPE structural integrity in the absence of F3. In congruence with suggestions from previously reported EM data [3], our analysis of RPE by ZO-1 staining revealed no structural deformities with respect to cell density (Fig. 5e, f; WT = 2432 ± 461 cells/mm^2, F3−/− = 2639 ± 443 cells/mm^2)(n =4–5) or number of neighboring cells (Fig. 5e, g; WT = 6.3 ± 0.2 cells, F3−/− =5.9 ± 0.6cells)(n =4–5) in F3−/− mice compared with WT at 15 months.

Ocular physiology remains functional in the absence of F3

After confirming that the absence of F3 causes no structural deficits in the TM/ciliary body, retina, RPE, and optic nerve, we evaluated whether the lack of F3 is accompanied by any physiological changes in the eye. To this end, we measured IOP to assess changes in aqueous humor dynamics as a function of the ciliary body and TM. We observed that F3−/− animals exhibited lower IOPs compared with WT ((WT = (OD) 18.6 ± 2.6 mm of Hg, (OS) 19.2 ± 0.4 mm of Hg; F3−/− =(OD) 14.7 ± 1.7 mm of Hg, (OS) 14.8 ± 1.4 mm of Hg) at 6 months (n =4–5, p < 0.01 for OD and OS, 2-way ANOVA) (Supp. Fig. 3c). However, we believe that the IOPs recorded in the F3−/− animals are an underestimation of the actual readings. This is because we used a rebound tonometer to measure IOP, which would likely give an artificially low reading due to a thinner cornea [43]. Additionally, we would expect that true IOP changes would structurally alter the retina and optic nerve, which we do not observe. Thus, we believe that there are no true changes in IOP between WT and F3−/− mice.

Thus far, we have found no structural changes to the posterior segment due to the lack of F3. Yet, no one has attempted to look at functional modifications in the retina in the absence of F3. Therefore, we conducted physiological and functional tests to determine whether F3 plays any role in the functional workings of the retina. We used electroretinography (ERG) to examine the response to light stimulus in WT and F3−/− mice. No significant differences were observed in a-wave or b-wave scotopic response in the absence of F3 at 6 months (Fig.

6a, b). These results indicate that lack of F3 appears to neither affect visual signal transduction nor the electrical activity of the outer or inner retina.

We next set out to examine whether the electrical stimuli from the retina are being efficiently relayed to the visual centers of the brain. To test this, we measured optokinetic reflex (OKR) as a function of visual acuity [44, 45]. Our results suggest that the lack of F3 does not affect the visual pathway in the mouse as no differences were observed in visual acuity between WT and F3−/− mice at 2 months (WT 0.40 ± 0.02 cycles/o,F3/− 0.41 ± 0.03 cycles/o)(n =5) (Fig.6c). Supporting this notion, anterograde transport from the retina through the optic nerve was also unaffected in the absence of F3 as demonstrated by CTB-594 labeling of the nerve fiber layer in WT and F3−/− animals at 6 months (Fig. 6d, e).

Overall, the retinas of F3−/− mice are structurally and functionally intact, with no observable changes that can be attributed to the lack of F3. These data suggest that, unlike in the cornea, the absence of F3 in the TM, retina, RPE, and optic nerve is well-tolerated and does not disrupt structural or functional homeostasis in these tissues.

F3−/− mouse retina observations are corroborated by fundus imaging and OCT of a human patient with loss-of-function mutations in F3

Recently, two sets of unrelated individuals were identified to harbor either homozygous (p.C55R, two siblings) or biallelic (p.Met107fs, p.Tyr205*) loss-of-function mutations in F3 [31, 32]. All these patients presented with Marfan-like pathology, including tall stature, canonical facial presentation (long face and high, narrow palate), herniation, and overall connective tissue disruption. A cursory analysis suggested that the only apparent ocular defects in these patients were high, progressive myopia and astigmatism. To more definitively conclude that absence of F3 does not lead to structural disruption of the mammalian retina, we performed a thorough retinal analysis of the patient previously identified with biallelic mutations in F3 [31]. The patient noted no past ocular history aside from progressive myopia. This individual had a best-corrected vision of 6/12 (OD) and 6/7.5 (OS). Fundus (Fig. 7a, b) and OCT scans of the macula (Fig. 7c–f) indicated that the retina was of normal thickness with no retinal breaks or detachments. Furthermore, a more targeted analysis of the optic discs, as well as the thickness of the nerve fiber, ganglion cell, and inner plexiform layers, were also essentially normal and unremarkable (Sup. Figs. 5, 6). These data, combined with our in-depth structural and functional evaluation of retina from WT vs. F3−/− mice, strongly suggest that removal of F3 has no detrimental effect on normal retinal physiology.

Discussion

We have demonstrated that fibulins are widely expressed in various ocular tissues with high expression of F3 in the anterior segment of the eye, especially in the cornea. In fact, F3 is by far the dominant fibulin found in the mouse cornea. The cornea is responsible for most of the focusing power of the eye, and structural changes in the cornea lead to changes in its transparency and ability to focus that have direct visual implications during development and adulthood [46]. In our study, F3−/− mice exhibited corneal changes in the form of stromal thinning, and emergence of abnormal blood vessels that worsened with age. Although the

molecular mechanisms underlying the considerable thinning of the stroma in F3−/− mice remain to be elucidated, one might speculate that lack of F3 directly affects the production or proper organization of stromal ECM components leading to the observed structural deficits [46]. Previous studies have suggested that F3 interacts with ECM enzymes and regulates proteoglycan turnover [1]. Therefore, ablation of F3 might lead the disruption of both structural and functional integrity of corneal ECM leading to severe stromal thinning, as also observed in lumican-null mice exhibiting similar corneal phenotype [47].

Not much is known about the long-term ocular implications of F3 loss in human subjects. Two recent clinical reports of young adult patients with presumable loss-of-function mutations in the EFEMP1 gene indicate that they present with Marfan-like symptoms, connective tissue–related disorders, and several hernias, while the only reported ophthalmic manifestations were myopia and astigmatism [31, 32]. Our findings in one of these patients suggest that the retina of individuals lacking functional F3 is likely to be normal. Interestingly, children and adolescents with Marfan syndrome have also been reported to have thinner corneas and increased corneal astigmatism [48]. Furthermore, our data in mice suggest that with age, corneal changes in EFEMP1 loss-of-function humans could become apparent and may include opacification and vascularization. While prior studies with F3−/− animals did not thoroughly analyze the cornea, macroscopically, aside from periocular tumors [3], they appeared to be normal. The difference between our observations and previous findings might be due to strain differences in the animals used, as prior studies were performed on mixed backgrounds while we used C57BL/6 animals for all our studies. Interestingly, another study of a patient with the R345W F3 mutation reported corneal opacification and cloudiness in a human subject [49], bolstering the possibility of F3's importance in the cornea.

We were intrigued by the observation of a well-functioning posterior segment in F3−/− animals. Throughout the retina, we see intact structures and physiologic measurements. Our big-gest surprise was the low levels of F3 expression in the RPE/choroid, a region where pathological effects of mutant F3 (i.e., BLamDs, drusen) have been previously reported. Gain-of-function toxicity likely due to protein misfolding has been shown in the mouse model of ML to cause BLamDs [24, 25], and it has been proposed that mutant F3 causes retention of materials in Bruch's membrane, disrupting the function of the RPE and outer retina leading to disease [50]. However, no such changes were observed in the F3−/− animals in the absence of F3. This means that even though F3 is expressed in the neural retina, RPE/choroid, and optic nerve, removing it does not have detrimental effects in these tissues. This may be due to other fibulins being functionally redundant in the posterior segment and compensating for the loss of F3. It is also important to consider that F3 expression (as well as other fibulins) may be species-specific and that the expression pattern we observe in mice may be different in humans or non-human primates. Studies exploring these aspects should be considered before extrapolating the presented data to other species. Nevertheless, from our extensive study in mice, we observed no injurious effects on the neural retina, RPE, or optic nerve due to the absence of F3.

Our findings open up new avenues for gene therapy approaches by safely knocking out/ down F3 in the retina without having any adverse effects. Gene therapy for targeting mono-

genic inherited retinal diseases has been vastly pursued over the last decade [51], including the successful treatment and restoration of vision in Leber congenital amaurosis patients with RPE65 gene replacement therapy [52]. Such studies have paved the way for the development of safe and effective treatments for other inherited diseases through gene manipulation technology. Given the progress in adeno-associated virus (AAV) development, RNA interference, and CRISPR/Cas9 [53–55], gene therapies targeting F3 in the retina are viable strategies for the treatment of diseases like ML in the near future. By extension, due to the striking resemblance in pathological manifestations of ML and AMD, therapeutic approaches for ML targeting F3 may be extrapolated to treat the more prevalent disease, AMD, as well.

Materials and methods

Mice

C57BL/6 F3+/− mice were re-derived from stock provided by Dr. Lihua Marmorstein (Department of Ophthalmology and Vision Science, Mayo Clinic, Rochester, MN, USA). These mice were genotyped to confirm the absence of the Rd8, Rd1, and Gnat mutations. F3+/− breeding pairs were used to obtain WT, F3+/−, and F3−/− animals. The following primers were used for genotyping each of the mice by polymerase chain reaction (PCR): 5′-TCTCCGGAGAGCTCATAACC ACATG-3′ (common primer), 5′-GGAAGACAATAGCA GGCATGCTGGG-3′ (F3−/− primer), and 5′-TTCC TGAACATCAGAGTATTGGGAC-3′ (F3+/+,or WT primer)(Sup. Fig. 1a, b). The genotyping was also confirmed by qPCR using TaqMan and Sybr probes (Sup. Fig. 1c, d). All mice were maintained in 12-h/12-h light/dark cycle and sup-plied with food and water ad libitum. Equal numbers (n = mice) of age-matched, male and female littermates were used whenever possible. All experiments were conducted ethically in accordance with the ARVO Statement of the Use of Animals in Ophthalmic and Vision Research, UT Southwestern Medical Center (UTSW) Institutional Animal Care and Use Committee guidelines, and University of North Texas Health Science Center's Institutional Animal Care and Use Committee guidelines. For each experiment, comparative studies were initially performed between WT and F3−/− animals. F3+/− animals were used only when there were significant differences observed between WT and F3−/− animals to determine if the observed effect required complete absence of F3 or if ½ F3 expression was sufficient for the observed phenotype.

Quantitative PCR analysis

C57BL/6 WT animals were used to determine the levels of fibulins in various tissues. Mice were anesthetized using ketamine/xylazine cocktail (100/10 mg/kg) intraperitoneal (i.p.) injection. The brain, heart, lung, testes, and uterus were harvested, trimmed to a desirable size, and stored in RNAlater solution (Invitrogen #AM7020; Carlsbad, CA, USA) at 4 °C. Eyes were also harvested, ocular tissues dissected, and stored in RNAlater solution at 4 °C. RNA isolation was carried out using the Aurum Total RNA isolation kit (BioRad #732–6820; Hercules, CA, USA). Samples were reverse-transcribed to cDNA using qScript cDNA Supermix (Quantabio #101414–106; Beverly, MA, USA). TaqMan probes (Applied Biosystems; Waltham, MA, USA) were used for qPCR re-actions as follows: fibulin-1 (Mm00515700_m1), fibulin-2 (Mm00484266_m1), fibulin-3 (Mm00524588_m1), fibulin-4

(Mm00445429_m1), and fibulin-5 (Mm00488601_m1), and samples were run on a QuantStudio 6 Real-Time PCR system (Applied Biosystems #4485694) in technical and biological replicates. Relative abundance was calculated by comparing expression to β-actin (Mm02619580_g1) in each respective tissue.

In vivo confocal exam

WT, F3+/−, and F3−/− mice were anesthetized using ketamine/xylazine cocktail (100/10 mg/kg). Mouse corneas were evaluated using a modified Heidelberg Retinal Tomograph with Rostock Corneal Module (HRT-RCM; Heidelberg Engineering, GmBH, Dossenheim, Germany) in vivo confocal microscope with the Confocal Microscopy Through Focusing (CMTF) software as previously described [56, 57]. Since the reflection from the Tomocap can obscure images of the superficial epithelial cells, a thin PMMA (poly(methyl methacrylate)) washer was placed on the Tomocap as previously described [58, 59]. The objective was positioned on the cornea to create a flat field-of-view image in the central cornea. CMTF scans were collected by starting the scan in the anterior segment and finishing above the epithelium with a constant speed of 60 μm per second. Images were acquired with the rate set to 30 frames per second. To allow quantitative assessment of haze, scans were collected using a constant gain setting, by unchecking the "auto brightness" box in the HRT software interface. Each scan was conducted using a gain of 15 [60]. At least 3 scans were collected within the central area of the cornea Additional sequences were captured while maintaining focus on the superficial epithelium using auto gain settings. After image acquisition, CMTF scans were saved as ".vol" files, which could be opened using an in-house software to analyze the 3D changes in cell morphology and cell/ECM reflectivity [57]. The program generates an intensity vs. depth curve, corresponding to the average pixel intensity of each image and the z-depth of that image within the scan, respectively. The thicknesses of the stromal layer were calculated by the CMTF program using the interfaces (peaks on CMTF curve) between the basal lamina peak (or top of the stroma) and the endothelial peak. The average pixel intensity within the stromal layer was used as an indicator of stromal backscatter.

Slit-lamp imaging

WT, F3+/−, and F3−/− mice were anesthetized with isoflurane (2.5%) and oxygen (0.8 L/ minute). Anterior chamber phenotypes were assessed with a slit lamp (Haag-Streit Diagnostics #BQ-900; Mason, OH, USA) and documented with a digital camera (Canon EOS Rebel T6 DSLR, 18.0 megapixel CMOS image sensor and the DIGIC 4+ Image Processor). All images were taken using identical camera settings for brightness and contrast using the "auto-focus" option.

Spectral Domain-Optical Coherence Tomography

WT and F3−/− animals were anesthetized using ketamine/xylazine (100/10 mg/kg). Once unresponsive to foot pitch, the mouse was placed in a stage for SD-OCT (Bioptigen Envisu R2210; Morrisville, NC, USA). One drop of 1% tropicamide (Sandoz #61314–0355-02, West Princeton, NJ, USA) was placed on each eye to dilate the pupils, and GenTeal Tears gel (Alcon Laboratories Inc. # AL042947; Fort Worth, TX, USA) was applied to prevent the corneal surface from drying. The optic disc was located manually and was used to center the

scans. The retina was scanned at 1.8 mm × 1.8 mm 1000 × 100 × 10 and averaged to 1000 × 100 × 1. Images were analyzed using the Diver Software.

Initial preparation for histology and transmission electron microscopy (TEM)

Mice were anesthetized using ketamine/xylazine (100/10 mg/kg). Once unresponsive, mice were transcardially perfused with heparinized 1X PBS (10 units heparin per mL, Millipore Sigma #H5515; Burlington, MA, USA) followed by a fixative solution (2.5% (v/v) glutaraldehyde in 0.1 M sodium cacodylate buffer (Electron Microscopy Science (EMS) #100504–840; Hatfield, PA, USA)). Eyes were then harvested and processed for histological and TEM analyses as indicated below.

H&E histology

Enucleated eyes were processed for freeze substitution [61] as follows: briefly, eyes were rapidly frozen in isopentane for 1 min followed by incubation in 97% methanol and 3% acetic acid (MAA) at – 80 °C for 24–48 h, – 20 °C for 24–48 h, 4 °C for 24 h, and RT for at least 1 h. MAA was replaced with 100% ethanol, and the eyes were processed into paraffin-embedded sections (Histopathology Core, UT Southwestern). H&E staining was performed, and images of the sections were taken at × 25 magnification on either side of the optic nerve head using a Leica TCS SP8 confocal micro-scope (Leica Microsystems, Buffalo Grove, IL, USA). Unstained cross sections were also obtained to perform confirmatory immunohistochemistry on F3 localization in the retina.

Retinal ganglion cell quantification

Enucleated eyes were post fixed in 4% paraformaldehyde (PFA, (EMS #15710)) for 2 h at RT then washed with 1x PBS for 10 min (×3). Retinas were dissected and pre-treated in 0.3% TritonX-100 in PBS for 30 min (×4) and then blocked in 0.3% Triton X-100 (Fisher Scientific, #BP151, Pittsburgh, PA, USA) in PBS containing 10% goat serum (Gibco, #16210064, New Zealand origin) for 2 h. RGCs were labeled using anti-RNA-Binding Protein With Multiple Splicing (RBPMS, 1:1000, EMD Millipore #ABN1376; Burlington, MA, USA) antibody overnight at 4 °C. Following washes in PBS, the retinas were incubated with anti-rabbit AlexaFluor594 secondary antibody (1:1000, Invitrogen #A-11012) diluted in PBS with Tween 80 (Fisher Scientific, #BP338–500) overnight at 4 °C and mounted with Vectashield Mounting Medium containing 4′,6-diamidino-2-phenylindole (DAPI, Vector Laboratories #H-1200; Burlingame, CA, USA). Three images each were taken from the peripheral, mid-peripheral, and central regions of the four quadrants of each retina (12 images in total per retina) by confocal microscopy at × 25 magnification. Cells were counted by using the ImageJ (FIJI, Git version 2) Cell Counter Plugin as previously described [62]. For each individual retina, RGC density was obtained by averaging the 12 quadrant counts.

ZO-1 staining

Enucleated eyes were post fixed in 10% formalin for 10 min followed by washes in 1x PBS for 5 min (×3). The posterior eye cup was dissected, and the neural retina was separated from the RPE/choroid. The eye cup was then flatmounted and incubated in blocking buffer consisting of 1% BSA in 0.1% Triton X-100 in PBS for 1 h at RT. RPE tight junctions were

stained using an anti-ZO-1 (1:100, Invitrogen #40–2200) antibody in blocking buffer for 16 h at RT, then washed with 1x PBS for 5 min (×3). The flatmounts were then incubated in secondary antibody in blocking buffer anti-rabbit AlexaFluor488 secondary antibody (1:1000, Invitrogen #A27034) diluted in PBS with Tween 80 for 1 h at RT and mounted with ProLong Diamond Antifade medium containing DAPI (Life Technologies #P36961, Carlsbad, CA, USA). Eight images per retina were acquired at × 25 magnification using confocal microscopy. The Cellprofiler pipeline (version 2.2.1) was used to analyze RPE integrity as previously described [63].

Iba-1 and GFAP staining

Mice were euthanized by ketamine/xylazine overdose. Eyes were enucleated and fixed for 2 h in 4% paraformaldehyde at room temperature, then rinsed in PBS. Retinas were then dissected and pre-treated in 0.3%Triton X-100 in PBS for 30 min (×4) and then blocked in 0.3% Triton X-100 in PBS containing 10% goat serum (Gibco) for 2 h at RT. Microglia were labeled using anti-Iba-1antibody(1:500; #019–19741, Wako (Madison, WI)), and astrocytes were labeled using anti-GFAP antibody (1:500, #13–0300, Fisher Scientific) overnight at 4 °C. Following washes in PBS, the retinas were incubated with AlexaFluor488 goat-anti-rabbit (1:1000, #A-11008, Invitrogen, diluted in PBS with Tween) and AlexaFluor633 goat-anti-rat (1:1000, #A-21094, Invitrogen, diluted in PBS with Tween) overnight at 4 °C and mounted using ProLong Diamond Antifade Mountant (Invitrogen). Two Z-stack (2 μm × 25 steps) images were taken at × 25 magnification from peripheral, and central regions of the four quadrants of each retina using a confocal microscope. The images were Z-projected for maximum intensity using ImageJ (FIJI), and Iba-1 positive cells were counted separately in the inner retina and outer retina using trainable Weka segmentation plugin as previously described [64]. Briefly, a Z-projected image was loaded into ImageJ and subjected to Weka segmentation that out-lines microglia cell bodies. The image was then run through auto-threshold and converted to a binary image. By applying appropriate particle parameters (size, circularity), the Analyze particle command was run which gave the output of cell out-line and cell count. For each individual retina, the microglia cell count was obtained by averaging counts for inner and outer retina. Two-way ANOVA statistical analysis was performed to compare cell densities in WT and F3–/– retinas. For GFAP quantification, Z-projected images were loaded into ImageJ; threshold was applied and total intensities were measured. Unpaired t test was performed to compare WT and F3–/– retinas.

Corneal flatmounts

Mice were euthanized by ketamine/xylazine overdose. Eyes were enucleated and fixed for 2 h in 4% paraformaldehyde at room temperature, then rinsed in PBS. Corneas were then dissected and pre-treated in 0.3% Triton X-100in PBS for30min(×4) andthenblockedin0.3% TritonX-100 in PBS containing 10% goat serum (Gibco) for 2 h at RT. Limbal stem cells were labeled using anti-K15 antibody (1:250; #MA5–11344, Invitrogen), and proliferating cells were labeled using anti-Ki67 antibody (1:250, #14–5698-82, Invitrogen) overnight at 4 °C. Following washes in PBS, the corneas were incubated with AlexaFluor488 goat-anti-rat (1:1000, #A-11006, Invitrogen, diluted in PBS with Tween) and AlexaFluor594 goat-anti-mouse (1:1000, #A-11032, Invitrogen, diluted in PBS with Tween) overnight at 4 °C. The corneas were counter stained with DAPI and mounted (endothelium side up) using ProLong

Diamond Antifade Mountant (Invitrogen). Two Z-stack (2 μm x 25 steps) images were taken at 25x magnification from the limbal area of each cornea (n = 4) using confocal microscopy. The images were Z-projected for maximum intensity.

Transmission electron microscopy (TEM)

Enucleated eyes were fixed with 2.5% (v/v) glutaraldehyde in 0.1 M sodium cacodylate buffer (EMS #100504–840) (pH 7.4) for at least 2 h. After three rinses with 0.1 M sodium cacodylate buffer, samples were embedded in 3% agarose (w/v) and sliced into small blocks, rinsed with the same buffer three times, and post fixed with 1% osmium tetroxide and 0.8 % potassium ferricyanide (Millipore Sigma #13746–66-2) in 0.1 M sodium cacodylate buffer for 1.5 h at room temperature. Blocks were rinsed with water and with increasing concentration of ethanol, transitioned into propylene oxide (Millipore Sigma #540048), infiltrated with Embed-812 resin (EMS #14120) and polymerized in a 60 °C oven overnight. Blocks were sectioned with a diamond knife (Diatome) on a Leica Ultracut 7 ultramicrotome (Leica Microsystems) and collected onto formvar-coated slot grids, post stained with 2% aqueous uranyl acetate and lead citrate (Millipore Sigma #15326). Images were acquired at a magnification of $\times$ 300 on a JEOL 1400 Plus transmission electron micro-scope (JEOL) equipped with a LaB6 source using a voltage of 120 kV.

Axonal transport

Mice were anesthetized using ketamine/xylazine (100/10 mg/kg). A total of 1.5 μL of cholera toxin-B conjugated to AlexaFluor-594 (CTB-594; Life Technologies) was bilaterally injected into the posterior chamber using a 33-G needle attached to a 5-μLHamiltonsyringe (Hamilton company #600; Reno, NV, USA). Forty-eight hours later, the eyes along with the optic nerves were harvested and post fixed in 4% PFA for 2 h then washed in 1x PBS for 5 min (×3). Retinas were dissected, flatmounted, and examined under a confocal microscope using the × 10 objective. Optic nerves were cryoprotected in a sequential sucrose gradient in 1x PBS (10% for 12 h, followed by 20% for 12 h) and embedded in OCT cutting medium. The optic nerves were longitudinally sectioned at 14-μm thickness using a Leica CM3050 cryostat (Leica Microsystems) and imaged using the × 10 objective.

Intraocular pressure measurement

IOPs were measured in anesthetized animals (isoflurane, 2.5%; oxygen, 0.8 L/min) using a TonoLab rebound tonometer (Colonial Medical Supply, Franconia, NH, USA). Night-time IOPs were recorded in a masked manner in the early morning prior to the lights switching on for the day. An average of six IOP readings were recorded at each time point.

Electroretinogram (ERG)

WT and F3−/− mice were evaluated by full-field ERG (Ganzfeld ERG, Phoenix Instruments; Pleasanton, CA, USA) for response to light stimulus. Mice were dark-adapted overnight followed by anesthetizing with ketamine/xylazine and pupil dilation with 1%tropicamide (Sandoz #61314–0355-02, West Princeton, NJ, USA). The procedure was performed under dim, indirect red-light conditions. Three electrodes were placed at different locations on each mouse: a recording electrode attached to the camera was placed on one eye, and needle

electrodes were placed subcutaneously into the scalp (reference), and in the tail (ground). A Ganzfeld dome was used to expose the dark-adapted eye to a series of full-field flash stimuli ranging from -1.7 to 3.1 logcd*s/m2. With increasing light intensity, the interstimulus interval increased from 7 to 75 s, and the flashes were averaged to generate a waveform for each flash intensity. The analysis of the voltage tracings was accomplished using the LabScribe software (Phoenix Research Labs; Pleasanton, CA, USA).

OptoMotry

Optokinetic reflexes of WT and F3−/− mice were evaluated using a virtual optomotor system (OptoMotry; Cerebral Mechanics, White Plains, NY, USA), as described previously. Briefly, the spatial frequency threshold of freely moving mice on a platform was determined at maximum contrast (100%) by using a staircase method beginning with a minimum preset frequency of 0.050 cycles/degree. The thresholds were identified as the highest values that still elicited a following response in the mouse. Spatial frequency for at least 4 mice in each group was averaged and evaluated. The investigator was masked for the experiments.

Ethics and consent (human patient)

The individual described in this work was characterized previously [31] and consented to participate in a research study under approved protocols MEC/08/08/094 and 12/STH/56 (Health and Disability Ethics Committee, New Zealand).

Retinal exam of individual with loss-of-function mutations in F3

A patient who was previously identified as having biallelic loss-of-function mutations in F3 (p.Met107fs, p.Tyr205*, [31]) was referred to a local hospital (Southland Hospital, Invercargill, New Zealand) for an in-depth retinal exam. Fundus (Zeiss Clarus) and OCT images (Canon OCT-HS100, Canon, Tokyo, Japan) were obtained and processed to assess for indications of altered structural indicative of retinal degeneration and/or glaucoma. An in-depth corneal analysis was not performed due to scheduling and timing limitations.

Supplementary Material

Refer to Web version on PubMed Central for supplementary material.

Acknowledgments

References

1. Zhang Y, Marmorstein LY (2010) Focus on molecules: fibulin-3 (EFEMP1). Exp Eye Res 90:374–375 [PubMed: 19799900]

2. Hulleman JD (2016) Malattia Leventinese/Doyne honeycomb retinal dystrophy: similarities to age-related macular degeneration and potential therapies. Adv Exp Med Biol 854:153–158 [PubMed: 26427406]

3. McLaughlin PJ, Bakall B, Choi J, Liu Z, Sasaki T, Davis EC, Marmorstein AD, Marmorstein LY (2007) Lack of fibulin-3 causes early aging and herniation, but not macular degeneration in mice. Hum Mol Genet 16:3059–3070 [PubMed: 17872905]

4. Papke CL, Yanagisawa H (2014) Fibulin-4 and fibulin-5 in elastogenesis and beyond: Insights from mouse and human studies. Matrix Biol 37:142–149 [PubMed: 24613575]

5. Kumra H, Nelea V, Hakami H, Pagliuzza A, Djokic J, Xu J, Yanagisawa H, Reinhardt DP (2019) Fibulin-4 exerts a dual role in LTBP-4L-mediated matrix assembly and function. Proc Natl Acad Sci U S A 116:20428–20437 [PubMed: 31548410]

6. Li J, Qi C, Liu X, Li C, Chen J, Shi M (2018) Fibulin-3 knockdown inhibits cervical cancer cell growth and metastasis in vitro and in vivo. Sci Rep 8:10594 [PubMed: 30006571]

7. Nandhu MS, Kwiatkowska A, Bhaskaran V, Hayes J, Hu B, Viapiano MS (2017) Tumor-derived fibulin-3 activates pro-invasive NF-kappaB signaling in glioblastoma cells and their microenvironment. Oncogene 36:4875–4886 [PubMed: 28414309]

8. Tian H, Liu J, Chen J, Gatza ML, Blobe GC (2015) Fibulin-3 is a novel TGF-beta pathway inhibitor in the breast cancer microenvironment. Oncogene 34:5635–5647 [PubMed: 25823021]

9. Kim IG, Kim SY, Choi SI, Lee JH, Kim KC, Cho EW (2014) Fibulin-3-mediated inhibition of epithelial-to-mesenchymal transition and self-renewal of ALDH+ lung cancer stem cells through IGF1R signaling. Oncogene 33:3908–3917 [PubMed: 24013232]

10. Klenotic PA, Munier FL, Marmorstein LY, Anand-Apte B (2004) Tissue inhibitor of metalloproteinases-3 (TIMP-3) is a binding part-ner of epithelial growth factor-containing fibulin-like extracellular matrix protein 1 (EFEMP1). Implications for macular degenerations. J Biol Chem 279:30469–30473 [PubMed: 15123717]

11. Kobayashi N, Kostka G, Garbe JH, Keene DR, Bachinger HP, Hanisch FG, Markova D, Tsuda T, Timpl R, Chu ML et al. (2007) A comparative analysis of the fibulin protein family. Biochemical characterization, binding interactions, and tissue localization. J Biol Chem 282:11805–11816 [PubMed: 17324935]

12. Hulleman JD, Genereux JC, Nguyen A (2016) Mapping wild-type and R345W fibulin-3 intracellular interactomes. Exp Eye Res 153: 165–169 [PubMed: 27777122]

13. Blackburn J, Tarttelin EE, Gregory-Evans CY, Moosajee M, Gregory-Evans K (2003) Transcriptional regulation and expression of the dominant drusen gene FBLN3 (EFEMP1) in mammalian retina. Invest Ophthalmol Vis Sci 44:4613–4621 [PubMed: 14578376]

14. Stone EM, Lotery AJ, Munier FL, Heon E, Piguet B, Guymer RH, Vandenburgh K, Cousin P, Nishimura D, Swiderski RE et al. (1999) A single EFEMP1 mutation associated with both Malattia Leventinese and Doyne honeycomb retinal dystrophy. Nat Genet 22:199–202 [PubMed: 10369267]

15. Sohn EH, Wang K, Thompson S, Riker MJ, Hoffmann JM, Stone EM, Mullins RF (2015) Comparison of drusen and modifying genes in autosomal dominant radial drusen and age-related macular degeneration. Retina 35:48–57 [PubMed: 25077532]

16. Michaelides M, Jenkins SA, Brantley MA Jr, Andrews RM, Waseem N, Luong V, Gregory-Evans K, Bhattacharya SS, Fitzke FW, Webster AR (2006) Maculopathy due to the R345W substitution in fibulin-3: distinct clinical features, disease variability, and extent of retinal dysfunction. Invest Ophthalmol Vis Sci 47:3085–3097 [PubMed: 16799055]

17. Hulleman JD, Kaushal S, Balch WE, Kelly JW (2011) Compromised mutant EFEMP1 secretion associated with macular dystrophy remedied by proteostasis network alteration. Mol Biol Cell 22:4765–4775 [PubMed: 22031286]

18. Hulleman JD, Balch WE, Kelly JW (2012) Translational attenuation differentially alters the fate of disease-associated fibulin proteins. FASEB J 26:4548–4560 [PubMed: 22872678]

19. Marmorstein LY, Munier FL, Arsenijevic Y, Schorderet DF, McLaughlin PJ, Chung D, Traboulsi E, Marmorstein AD (2002) Aberrant accumulation of EFEMP1 underlies drusen formation in Malattia Leventinese and age-related macular degeneration. Proc Natl Acad Sci U S A 99:13067–13072 [PubMed: 12242346]

20. Hulleman JD, Brown SJ, Rosen H, Kelly JW (2013) A high-throughput cell-based Gaussia luciferase reporter assay for identifying modulators of fibulin-3 secretion. J Biomol Screen 18:647–658 [PubMed: 23230284]

21. Hulleman JD, Kelly JW (2015) Genetic ablation of N-linked gly-cosylation reveals two key folding pathways for R345W fibulin-3, a secreted protein associated with retinal degeneration. FASEB J 29: 565–575 [PubMed: 25389134]

22. Roybal CN, Marmorstein LY, Vander Jagt DL, Abcouwer SF (2005) Aberrant accumulation of fibulin-3 in the endoplasmic reticulum leads to activation of the unfolded protein response and VEGF expression. Invest Ophthalmol Vis Sci 46:3973–3979 [PubMed: 16249470]

23. Fernandez-Godino R, Garland DL, Pierce EA (2015) A local complement response by RPE causes early-stage macular degeneration. Hum Mol Genet 24:5555–5569 [PubMed: 26199322]

24. Fu L, Garland D, Yang Z, Shukla D, Rajendran A, Pearson E, Stone EM, Zhang K, Pierce EA (2007) The R345W mutation in EFEMP1 is pathogenic and causes AMD-like deposits in mice. Hum Mol Genet 16:2411–2422 [PubMed: 17666404]

25. Marmorstein LY, McLaughlin PJ, Peachey NS, Sasaki T, Marmorstein AD (2007) Formation and progression of sub-retinal pigment epithelium deposits in Efemp1 mutation knock-in mice: a model for the early pathogenic course of macular degeneration. Hum Mol Genet 16:2423–2432 [PubMed: 17664227]

26. Garland DL, Fernandez-Godino R, Kaur I, Speicher KD, Harnly JM, Lambris JD, Speicher DW, Pierce EA (2014) Mouse genetics and proteomic analyses demonstrate a critical role for complement in a model of DHRD/ML, an inherited macular degeneration. Hum Mol Genet 23:52–68 [PubMed: 23943789]

27. Duvvari MR, van de Ven JP, Geerlings MJ, Saksens NT, Bakker B, Henkes A, Neveling K, del Rosario M, Westra D, van den Heuvel LP et al. (2016) Whole exome sequencing in patients with the cuticular drusen subtype of age-related macular degeneration. PLoS One 11:e0152047 [PubMed: 27007659]

28. Guymer RH, McNeil R, Cain M, Tomlin B, Allen PJ, Dip CL, Baird PN (2002) Analysis of the Arg345Trp disease-associated allele of the EFEMP1 gene in individuals with early onset drusen or familial age-related macular degeneration. Clin Exp Ophthalmol 30:419–423 [PubMed: 12427233]

29. Meyer KJ, Davis LK, Schindler EI, Beck JS, Rudd DS, Grundstad AJ, Scheetz TE, Braun TA, Fingert JH, Alward WL et al. (2011) Genome-wide analysis of copy number variants in age-related macular degeneration. Hum Genet 129:91–100 [PubMed: 20981449]

30. Mackay DS, Bennett TM, Shiels A (2015) Exome sequencing identifies a missense variant in EFEMP1 co-segregating in a family with autosomal dominant primary open-angle glaucoma. PLoS One 10: e0132529 [PubMed: 26162006]

31. Driver SGW, Jackson MR, Richter K, Tomlinson P, Brockway B, Halliday BJ, Markie DM, Robertson SP, Wade EM (2020) Biallelic variants in EFEMP1 in a man with a pronounced connective tissue phenotype. Eur J Hum Genet 28:445–452 [PubMed: 31792352]

32. Bizzari S, El-Bazzal L, Nair P, Younan A, Stora S, Mehawej C, El-Hayek S, Delague V, Megarbane A (2020) Recessive marfanoid syndrome with herniation associated with a homozygous mutation in Fibulin-3. Eur J Med Genet 63:103869 [PubMed: 32006683]

33. Hasegawa A, Yonezawa T, Taniguchi N, Otabe K, Akasaki Y, Matsukawa T, Saito M, Neo M, Marmorstein LY, Lotz MK (2017) Role of fibulin 3 in aging-related joint changes and osteoarthritis pathogenesis in human and mouse knee cartilage. Arthritis Rheum 69:576–585

34. Stanton JB, Marmorstein AD, Zhang Y, Marmorstein LY (2017) Deletion of Efemp1 is protective against the development of sub-RPE deposits in mouse eyes. Invest Ophthalmol Vis Sci 58:1455–1461 [PubMed: 28264101]

35. Timpl R, Sasaki T, Kostka G, Chu ML (2003) Fibulins: a versatile family of extracellular matrix proteins. Nat Rev 4:479–489

36. Yanagisawa H, Davis EC, Starcher BC, Ouchi T, Yanagisawa M, Richardson JA, Olson EN (2002) Fibulin-5 is an elastin-binding protein essential for elastic fibre development in vivo. Nature 415: 168–171 [PubMed: 11805834]

37. Tsunezumi J, Sugiura H, Oinam L, Ali A, Thang BQ, Sada A, Yamashiro Y, Kuro OM, Yanagisawa H (2018) Fibulin-7, a heparin binding matricellular protein, promotes renal tubular calcification in mice. Matrix Biol 74:5–20 [PubMed: 29730503]

38. Nasser W, Amitai-Lange A, Soteriou D, Hanna R, Tiosano B, Fuchs Y, Shalom-Feuerstein R (2018) Corneal-committed cells re-store the stem cell pool and tissue boundary following injury. Cell Rep 22:323–331 [PubMed: 29320729]

39. Fabiani C, Barabino S, Rashid S, Dana MR (2009) Corneal epithelial proliferation and thickness in a mouse model of dry eye. Exp Eye Res 89:166–171 [PubMed: 19298814]

40. Quigley HA (2011) Glaucoma. Lancet 377:1367–1377 [PubMed: 21453963]

41. Thompson S, Blodi FR, Larson DR, Anderson MG, Stasheff SF (2019) The Efemp1R345W Macular dystrophy mutation causes amplified circadian and photophobic responses to light in mice. Invest Ophthalmol Vis Sci 60:2110–2117 [PubMed: 31095679]

42. Wyatt MK, Tsai JY, Mishra S, Campos M, Jaworski C, Fariss RN, Bernstein SL, Wistow G (2013) Interaction of complement factor h and fibulin3 in age-related macular degeneration. PLoS One 8: e68088 [PubMed: 23840815]

43. Brubaker RF (1999) Tonometry and corneal thickness. Arch Ophthalmol 117:104–105 [PubMed: 9930168]

44. Douglas RM, Alam NM, Silver BD, McGill TJ, Tschetter WW, Prusky GT (2005) Independent visual threshold measurements in the two eyes of freely moving rats and mice using a virtual-reality optokinetic system. Vis Neurosci 22:677–684 [PubMed: 16332278]

45. Prusky GT, Alam NM, Beekman S, Douglas RM (2004) Rapid quantification of adult and developing mouse spatial vision using a virtual optomotor system. Invest Ophthalmol Vis Sci 45:4611–4616 [PubMed: 15557474]

46. Xuan M, Wang S, Liu X, He Y, Li Y, Zhang Y (2016) Proteins of the corneal stroma: importance in visual function. Cell Tissue Res 364:9–16 [PubMed: 26905288]

47. Chakravarti S, Petroll WM, Hassell JR, Jester JV, Lass JH, Paul J, Birk DE (2000) Corneal opacity in lumican-null mice: defects in collagen fibril structure and packing in the posterior stroma. Invest Ophthalmol Vis Sci 41:3365–3373 [PubMed: 11006226]

48. Salchow DJ, Gehle P (2019) Ocular manifestations of Marfan syndrome in children and adolescents. Eur J Ophthalmol 29:38–43 [PubMed: 29587526]

49. Zhang K, Sun X, Chen Y, Zhong Q, Lin L, Gao Y, Hong F (2018) Doyne honeycomb retinal dystrophy/malattia leventinese induced by EFEMP1 mutation in a Chinese family. BMC Ophthalmol 18: 318 [PubMed: 30541486]

50. Zayas-Santiago A, Cross SD, Stanton JB, Marmorstein AD, Marmorstein LY (2017) Mutant fibulin-3 causes proteoglycan accumulation and impaired diffusion across Bruch's membrane. Invest Ophthalmol Vis Sci 58:3046–3054 [PubMed: 28622396]

51. Bessant DA, Ali RR, Bhattacharya SS (2001) Molecular genetics and prospects for therapy of the inherited retinal dystrophies. Curr Opin Genet Dev 11:307–316 [PubMed: 11377968]

52. Simonelli F, Maguire AM, Testa F, Pierce EA, Mingozzi F, Bennicelli JL, Rossi S, Marshall K, Banfi S, Surace EM et al. (2010) Gene therapy for Leber's congenital amaurosis is safe and effective through 1.5 years after vector administration. Mol Ther 18:643–650 [PubMed: 19953081]

53. Jain A, Zode G, Kasetti RB, Ran FA, Yan W, Sharma TP, Bugge K, Searby CC, Fingert JH, Zhang F et al. (2017) CRISPR-Cas9-based treatment of myocilin-associated glaucoma. Proc Natl Acad Sci U S A 114:11199–11204 [PubMed: 28973933]

54. Wu J, Bell OH, Copland DA, Young A, Pooley JR, Maswood R, Evans RS, Khaw PT, Ali RR, Dick AD et al. (2020) Gene therapy for glaucoma by ciliary body aquaporin 1 disruption using CRISPR-Cas9. Mol Ther 28:820–829 [PubMed: 31981492]

55. Jo DH, Song DW, Cho CS, Kim UG, Lee KJ, Lee K, Park SW, Kim D, Kim JH, Kim JS et al. (2019) CRISPR-Cas9-mediated therapeutic editing of Rpe65 ameliorates the disease phenotypes in a mouse model of Leber congenital amaurosis. Sci Adv 5:eaax1210 [PubMed: 31692906]

56. Petroll WM, Kivanany PB, Hagenasr D, Graham EK (2015) Corneal fibroblast migration patterns during intrastromal wound healing correlate with ECM structure and alignment. Invest Ophthalmol Vis Sci 56:7352–7361 [PubMed: 26562169]

57. Petroll WM, Weaver M, Vaidya S, McCulley JP, Cavanagh HD (2013) Quantitative 3-dimensional corneal imaging in vivo using a modified HRT-RCM confocal microscope. Cornea 32:e36–e43 [PubMed: 23051907]

58. Cai D, Zhu M, Petroll WM, Koppaka V, Robertson DM (2014) The impact of type 1 diabetes mellitus on corneal epithelial nerve morphology and the corneal epithelium. Am J Pathol 184:2662–2670 [PubMed: 25102563]

59. Zhivov A, Stachs O, Stave J, Guthoff RF (2009) In vivo three-dimensional confocal laser scanning microscopy of corneal surface and epithelium. Br J Ophthalmol 93:667–672 [PubMed: 18650213]

60. Kivanany PB, Grose KC, Petroll WM (2016) Temporal and spatial analysis of stromal cell and extracellular matrix patterning following lamellar keratectomy. Exp Eye Res 153:56–64 [PubMed: 27732879]

61. Sun N, Shibata B, Hess JF, FitzGerald PG (2015) An alternative means of retaining ocular structure and improving immunoreactivity for light microscopy studies. Mol Vis 21:428–442 [PubMed: 25991907]

62. Daniel S, Clark AF, McDowell CM (2018) Subtype-specific response of retinal ganglion cells to optic nerve crush. Cell Death Dis 4:7

63. Boatright JH, Dalal N, Chrenek MA, Gardner C, Ziesel A, Jiang Y, Grossniklaus HE, Nickerson JM (2015) Methodologies for analysis of patterning in the mouse RPE sheet. Mol Vis 21:40–60 [PubMed: 25593512]

64. Ramadurgum P, Woodard DR, Daniel S, Peng H, Mallipeddi PL, Niederstrasser H, Mihelakis M, Chau VQ, Douglas PM, Posner BA et al. (2020) Simultaneous control of endogenous and user-defined genetic pathways using unique ecDHFR pharmacological chaperones. Cell Chem Biol 27:622–634 e626 [PubMed: 32330442]

Key messages

- Fibulins are expressed throughout the body at varying levels.

- Fibulin-3 has a tissue-specific pattern of expression within the eye.

- Lack of fibulin-3 leads to structural deformities in the cornea.

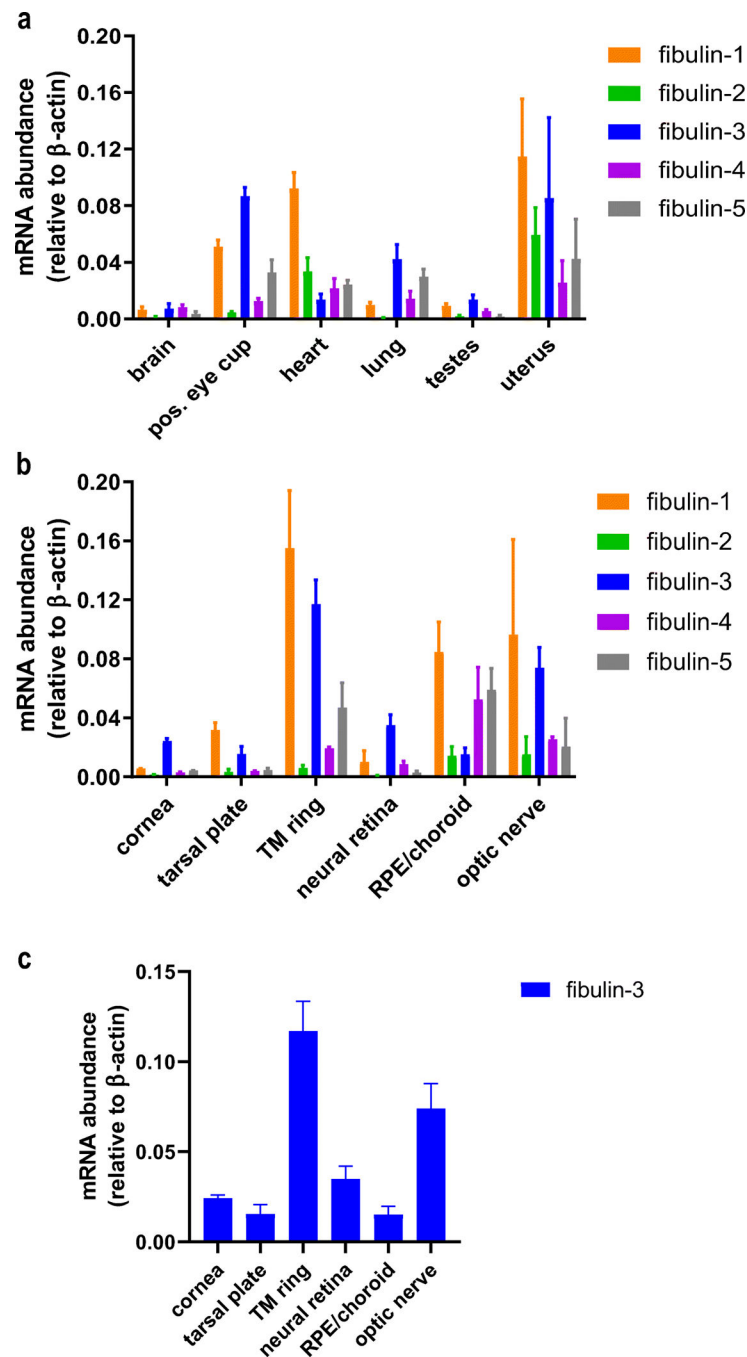- The retina and RPE remain structurally and functionally healthy in the absence of fibulin-3 in both mice and humans.

Fig. 1.
Gene expression profile of the fibulins. (a) Expression levels of fibulin 1–5 in brain, posterior (pos.) eye cup, heart, lung, testes, and uterus relative to β-actin. (b) Expression levels of fibulin 1–5 in ocular tissues, namely cornea, tarsal plate, trabecular meshwork (TM) ring, neural retina, RPE/choroid, and optic nerve relative to β-actin. c Reiteration of Fig. 1b focusing on the expression of F3 in ocular tissues. The values are represented as mean ± SD (n = 3–5)
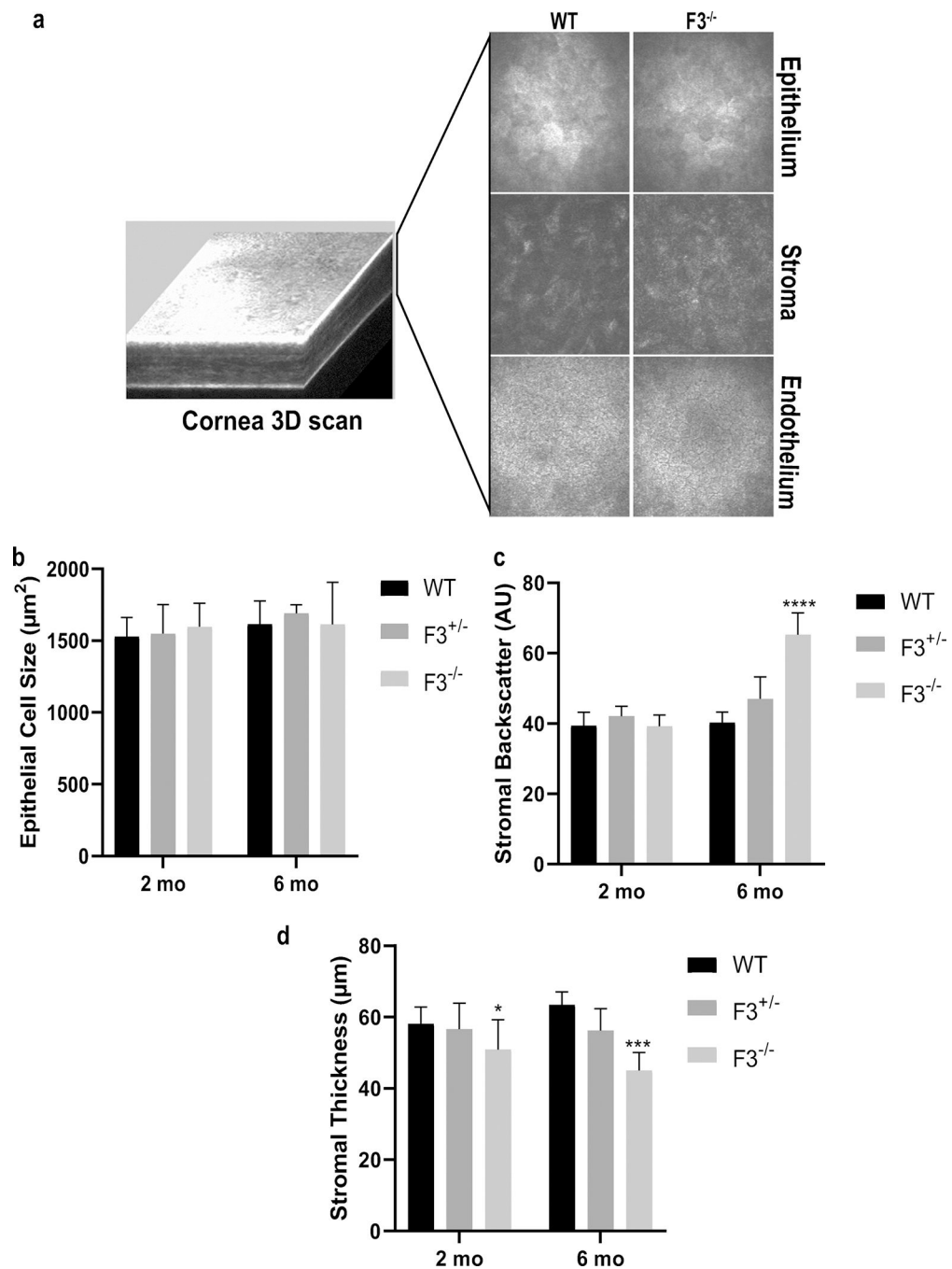
Fig. 2.
Lack of F3 leads to stromal thinning as well as increased corneal haze in F3−/− animals. (a) Representative image of in vivo 3D corneal scan. Panels showing comparative images of epithelial, stromal, and endothelial layers of WT and F3−/− animals. (b) Graph representing epithelial cell size (μm2) shows no differences between WT, F3+/−, and F3−/− in 2 month (n = 7–12) and 6 month (n = 4–7) animals. (c) Graph representing stromal backscatter (AU) displays no differences between WT, F3+/−, and F3−/− at 2 months (n = 7–12), while increased stromal backscatter is observed in F3−/− animals compared with that in WT at 6

months (n = 4–7, p < 0.0001). (d) Graph representing stromal thickness (μm) shows decreased thickness in F3−/− at 2months (n = 7–12, p = 0.02) and 6 months (n = 4–7, p < 0.001) compared with that in WT. Analyses performed by 2-way ANOVA and represented as mean ± SD
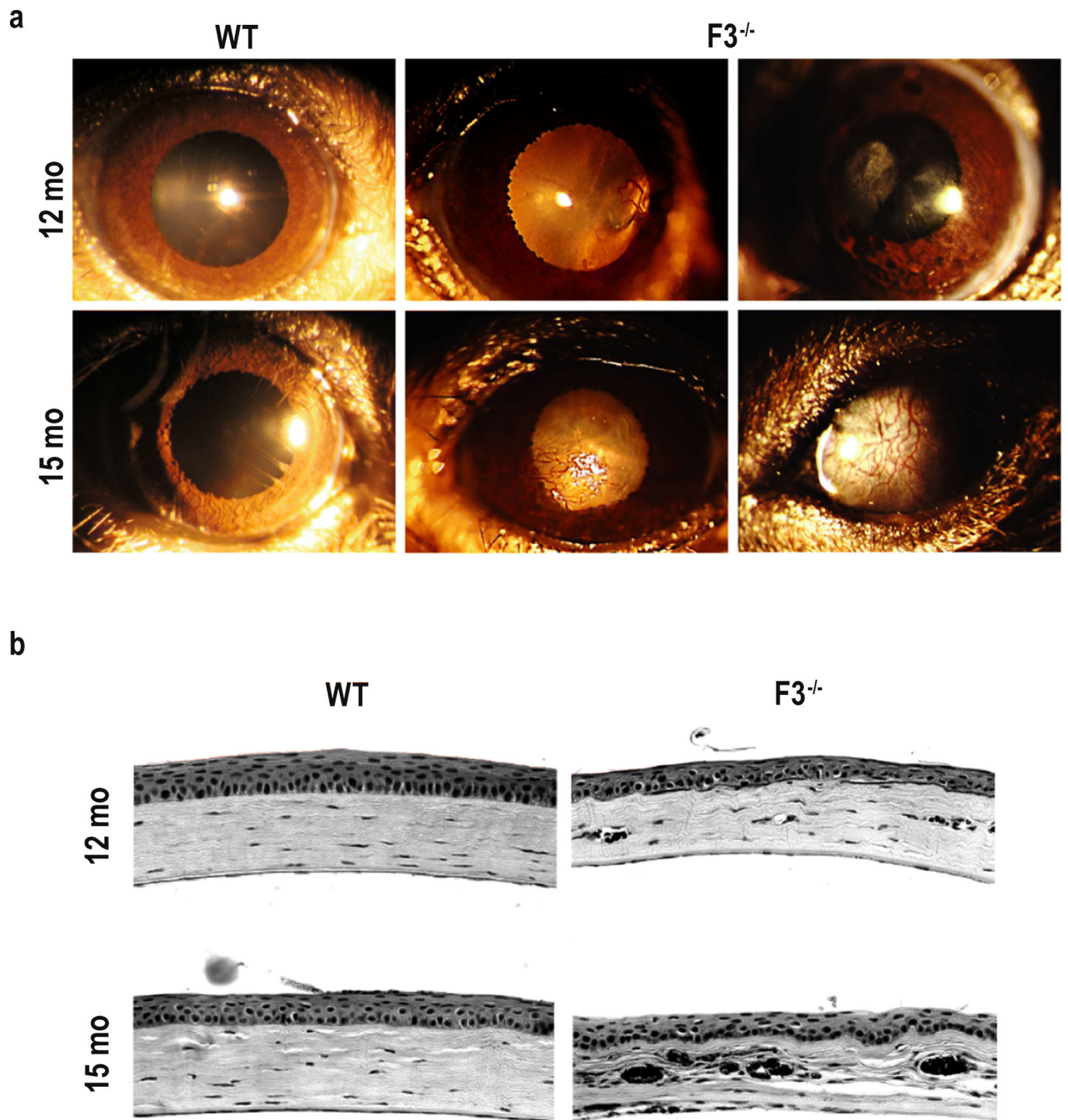
a

b

Fig. 3.
Corneal opacification, vascularization, and deterioration in F3−/− mice. (a) Representative images of slit-lamp examination. Panels depict various phenotypic manifestations of corneal changes in 12 months and 15 months F3−/− animals compared with WT (n = 4–6). (b) Corneal histology. Representative images showing histological changes in the cornea of F3−/− animals compared with that of WT at 12 months and 15 months (n = 4–5) (scale bar = 50 μm)
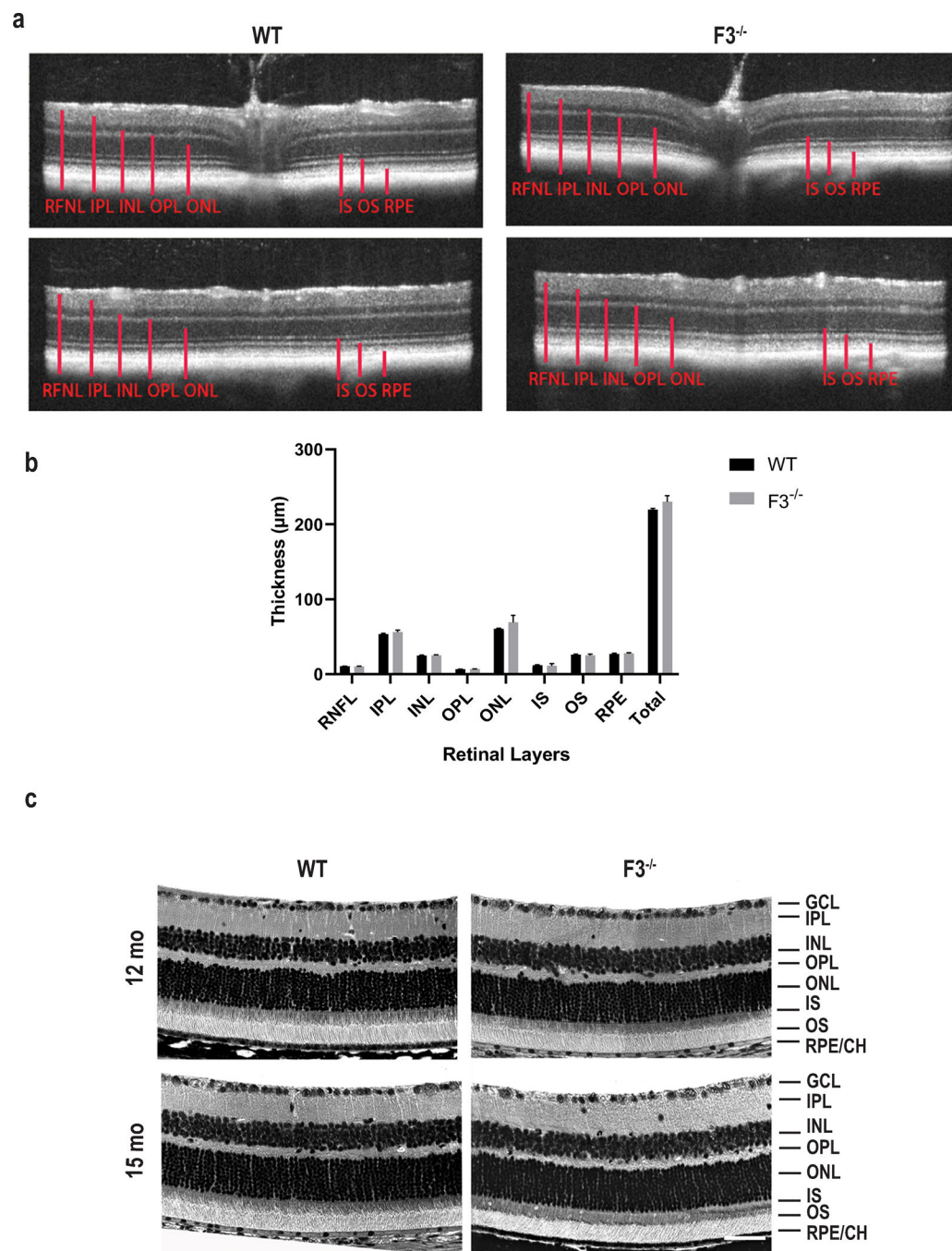
Fig. 4.
Retina remains structurally intact in the absence of F3. (a) Representative images of SD-OCT examination. SD-OCT scans of F3−/− and WT mice show no distinguishable changes in thickness for all the retinal layers at 9 months. Top panel represents scans from optic nerve head and bottom panels from the periphery. (b) Graph representing comparison of thickness of retinal layers between WT and F3−/− represented as mean ± SD. (c) Retinal histology. Representative images showing comparable histological structures in F3−/− and WT animals at 15 months (scale bar = 50 μm). RNFL retinal nerve fiber layer, GCL

ganglion cell layer, IPL inner plexiform layer, INL inner nuclear layer, OPL outer plexiform layer, ONL outer nuclear layer, IS inner segment, OS outer segment, RPE retinal pigment epithelium, CH choroid (n = 6–7)
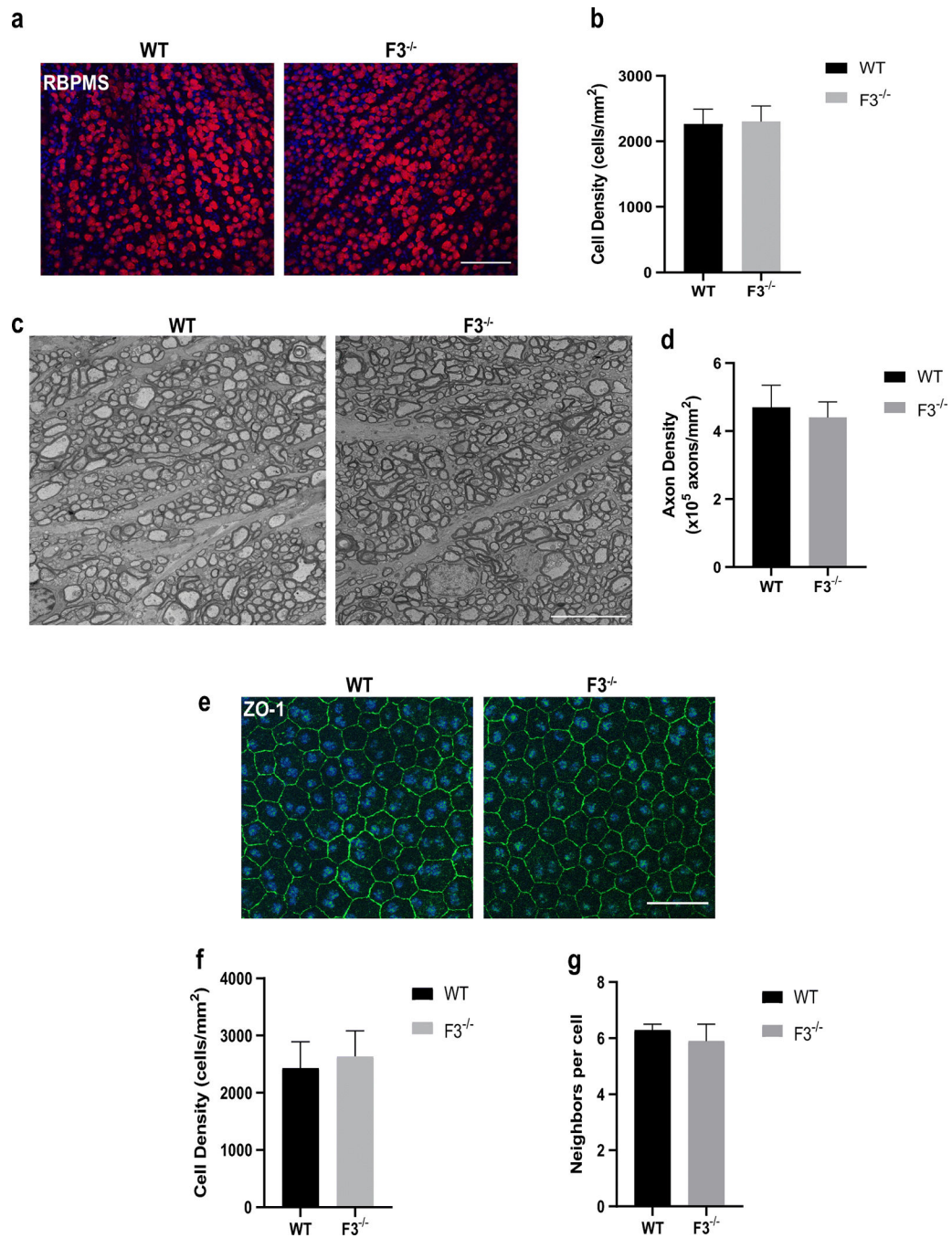
Fig. 5.

Ganglion cells, axons, and RPE appear unaffected in F3−/− animals. (a) Representative images of RGCs stained with RBPMS in WT and F3−/− mice at 15 months (scale bar = 100 μm). (b) Graph representing cell density (cells/mm2) shows no differences between WT and F3−/− 15 month mice (n = 5–6). (c) Representative images of optic nerve cross sections after electron microscopy of WT and F3−/− mice at 15 months (scale bar = 10 μm). (d) Graphical representation of axonal density ($\times 10^5$ axons/mm^2) shows no difference between WT and F3−/− (n = 3–4). (e) ZO-1 staining of RPE cells of WT and F3−/− in 15 month mice (scale

bar = 100 μm). (f) RPE cell density (cells/mm2). (g) Number of neighboring cells are similar in comparison for WT and F3−/− animals (n = 5–6). Analyses performed by 2-way ANOVA and represented as mean ± SD
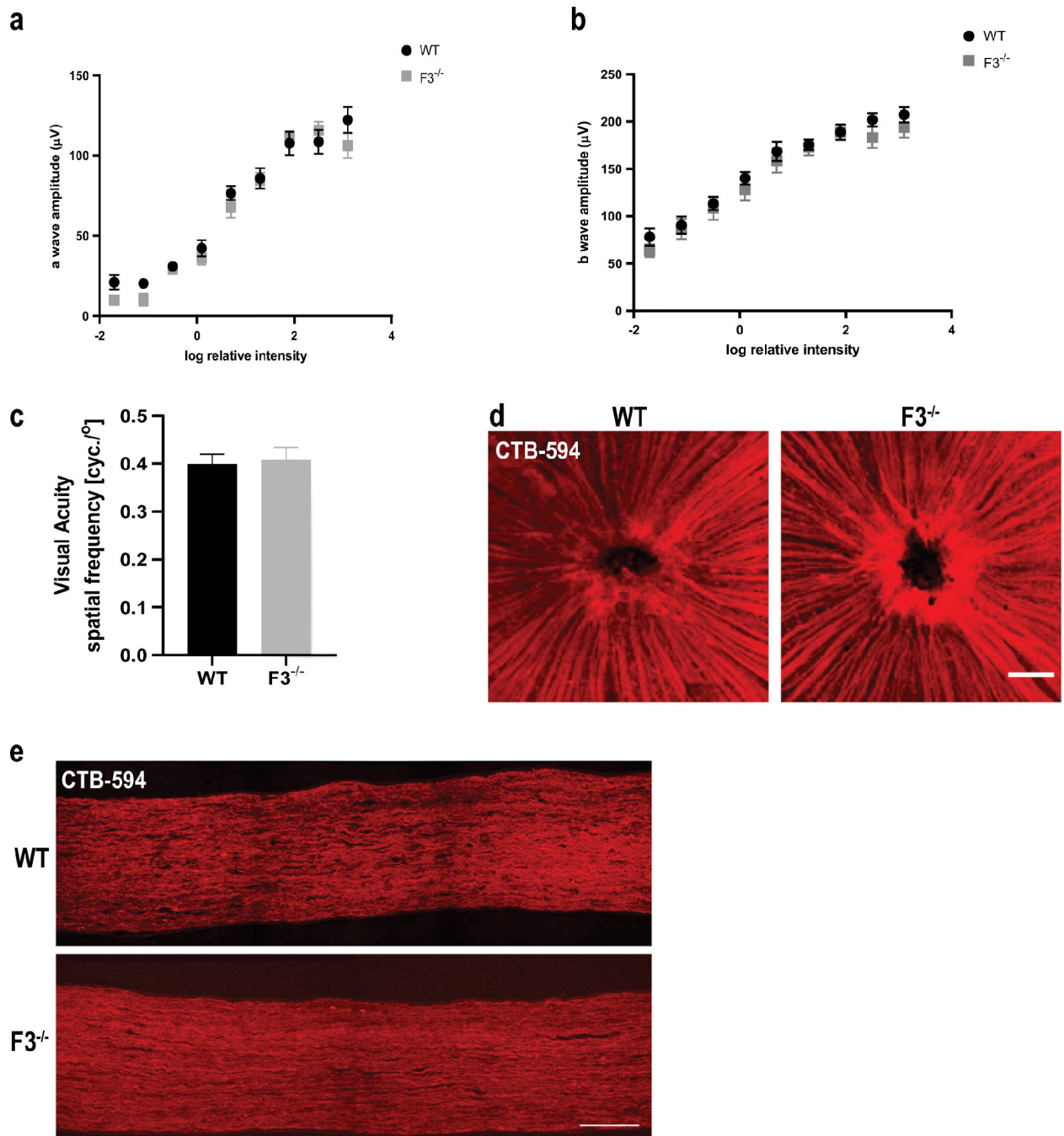
Fig. 6.

Normal retinal physiology and function are observed in the absence of F3. (a) An ERG exam revealed no significant differences in a-wave response (b) or b-wave response between WT and F3−/− animals at 6 months (n = 10–12 eyes). (c) Normal visual acuity was recorded for both WT and F3−/− animals by OKR at 2 months (n = 5). Analyses performed by 2-way ANOVA and represented as mean ± SD. (d) Representative images of CTB-594 tracer through nerve fiber layer (scale bar = 100 μm) and (e) optic nerve axons did not show any transport deficit in F3−/− mice compared with WT at 15 months (scale bar = 100 μm)
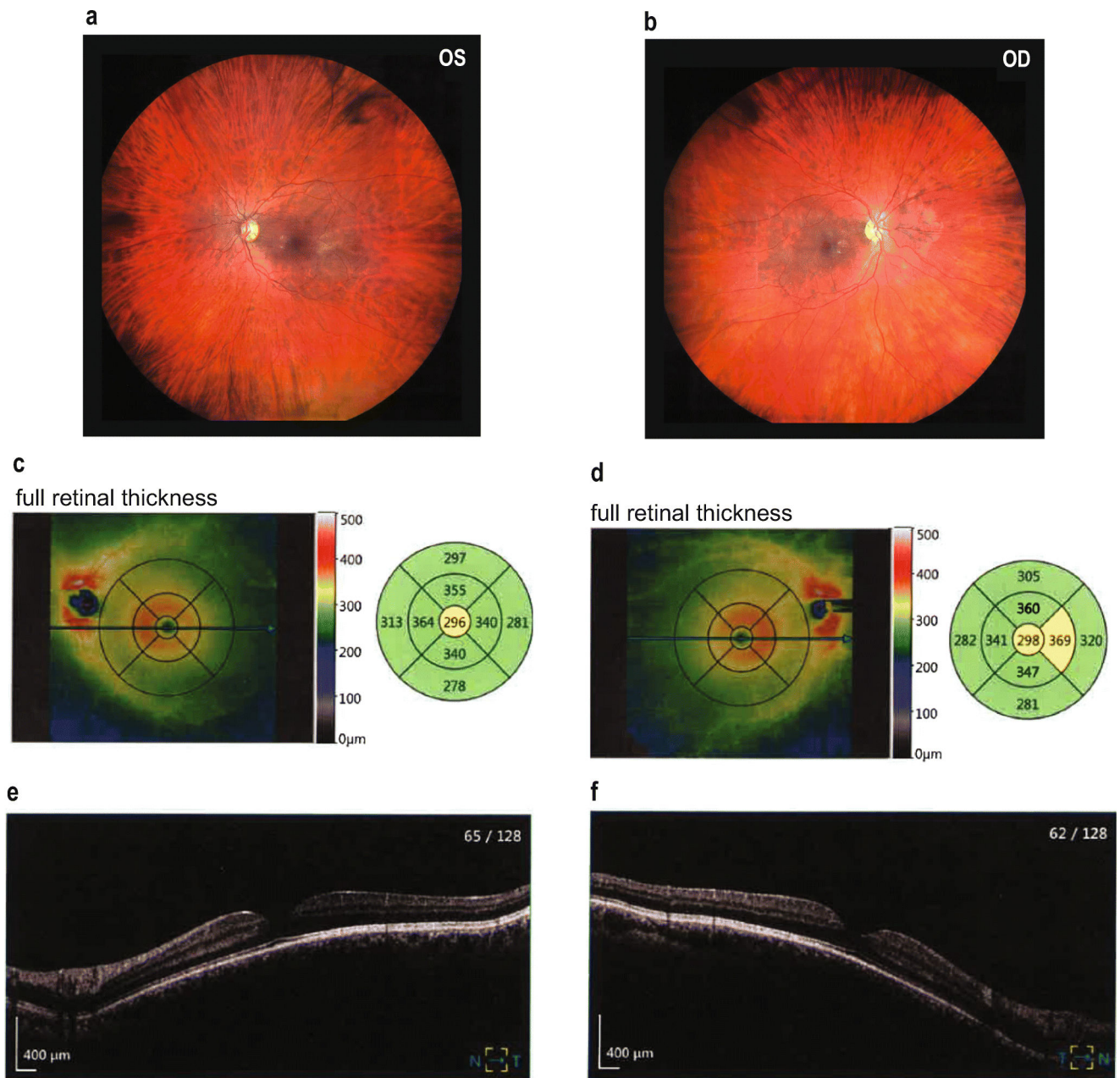
Fig. 7.
Normal retinal structure in a patient with biallelic loss-of-function mutations in F3. (a, b) Unremarkable fundus photographs from a patient that has mutations (p.(Met107fs, resulting in a premature stop codon at residue 127) and p.(Tyr205*)) on separate alleles encoding for F3. (c–f) OCT-mediated measurements demonstrate normal retinal thickness (average of 305 μm OS, 310 μm OD) and total retinal volume (8.64 mm^3 OS, 8.77 mm^3 OD)